Corrosion and tribocorrosion performance degradation mechanism of multilayered graphite-like carbon (GLC) coatings under deep-sea immersion in the western Pacific

Yingrui Liu [a,b,c], Guanshui Ma [a], Xin Ma [e], Hao Li [a], Peng Guo [a], Aiying Wang [a,d,*], Peiling Ke [a,d,*]

[a] *Key Laboratory of Advanced Marine Materials, Ningbo Institute of Materials Technology and Engineering, Chinese Academy of Sciences, Ningbo 315201, China*
[b] *Chongqing Institute of Green and Intelligent Technology, Chinese Academy of Sciences, Chongqing 400714, China*
[c] *Chongqing Institution of Bio-intelligent Manufacturing, Chongqing 401120, China*
[d] *Center of Materials Science and Optoelectronics Engineering, University of Chinese Academy of Sciences, Beijing 100049, China*
[e] *Physical Oceanography Laboratory, Ocean University of China, Qingdao 266100, China*

ARTICLE INFO

ABSTRACT

Corrosion evolution of Cr/GLC multilayered coating exposed in the deep sea of the western Pacific after 342 days at various depths was investigated. Results showed that the atomic structure of the top-layer GLC layer remained almost unchanged after immersion, but severe corrosion across multi-scaled interfaces was significantly stimulated as the immersion depth increased. This further led to the weakening of coating density and adhesion strength, with the wear rate and corrosion rate being two orders of magnitude larger than those of the as-deposited coating. Therefore, reducing defect density and conductivity is the key to designing GLC coatings for deep-sea applications.

1. Introduction

Graphite-like carbon (GLC) coating features significant sp2-hybridized carbon and a unique combination of favorable properties such as low friction coefficient, high hardness and chemical inertness [1, 2]. GLC coatings deposited by magnetron sputtering methods, the weak bonds between graphite layers exhibit minimal affinity for water molecule adsorption due to the absence of hydrogen [3]. As a result, its environmental sensitivity is greatly reduced [4,5] and suitable for aqueous lubrication environment application, such as the surface protective coatings on moving components in deep sea environments [6].

The complexity of the deep sea, characterized by high hydrostatic pressure and low temperatures, leads to an evolution in material performance due to their combined effects [7,8]. Among them, deep-sea hydrostatic pressure is the most important factor affecting the corrosion properties of materials [9]. Many researchers have employed laboratory simulations of the deep sea to investigate the effects of hydrostatic pressure on the corrosion behavior and mechanisms of different materials over short periods of time. Most of the results showed

that hydrostatic pressure promoted the corrosion process of materials in deep-sea environments. For example, hydrostatic pressure can accelerate the diffusion rate of seawater in the epoxy resin coating, reducing the protective properties of the coatings [10–12]. In the case of metallic materials, hydrostatic pressure reduces corrosion resistance by changing the structure and composition of the passivation film on the surface of the material [13,14]. The results of these laboratory studies have helped us to understand to some extent how hydrostatic pressure affects the corrosion properties of materials. Previously, our team also carried out a series of simulated deep-sea experiments with in-situ electrochemical tests to investigate the corrosion behavior of Cr/GLC multilayered coatings at 30 MPa (simulating a depth of 3000 m) [15]. It has been found that the localized corrosion resistance of the coating decreased under high hydrostatic pressure environment [16], which is closely related to the corrosion reaction occurred at the coating defect. It was also found that hydrostatic pressure promotes Cl^- adsorption on the coating surface, which together promotes dissolution of the Cr layer and the metal substrate [17]. These results show that hydrostatic pressure also has a significant negative effect on the corrosion resistance of

Cr/GLC coatings, especially on the densification of the coatings.

As a good solid lubricating coating material, the law of hydrostatic pressure on the tribological properties of GLC coatings is also of interest. The wear failure mechanism of GLC coatings under water lubrication conditions at atmosphere environment has been illustrated to the brittle fracture and delamination [18]. Consequently, the tribology properties of this coatings significantly depend on the adhesion strength at the metal/coating interface. In addition to understanding the pathways of hydrostatic pressure-accelerated corrosion reactions, it is essential to further investigate whether the hydrostatic pressure-accelerated corrosion process in the deep sea leads to changes in the adhesion strength. However, due to the limitations of the experimental equipment, most of the current studies on the effects of the corrosion behavior of materials in hydrostatic environments have been carried out over a relatively short period of time (e.g. 500 hours of immersion) [19]. The evolution of the corrosion and friction properties of the coating material at longer immersion times is even more important for GLC lubrication coatings.

However, no research has been reported on the performance evolution of carbon-based solid lubricating coating materials in real deep-sea environments. For this reason, this study employed a long-term exposure experiment at varying depths (500 m, 1500 m and 5942 m) in Pacific Ocean lasting 342 days. By combining analysis of the corrosion resistance, corrosion morphologies and tribology properties after exposure, the impact laws and mechanisms of actual deep-sea environments on the corrosion and tribology properties of GLC coatings were investigated comprehensively. This study aims to surpass laboratory simulation analyses and provide a more realistic and comprehensive understanding of the degradation mechanisms of metal/coating performance in actual deep-sea environments. Ultimately, it aims to establish the theoretical framework for enhancing GLC coatings' design for implementation in profound marine applications.

2. Experimental detail

2.1. Coating fabrication process

The Cr/GLC multilayered coatings were deposited with direct current magnetron sputtering (DCMS) using an alternate method on polished 17–4PH stainless steels (φ18 mm$\times$3 mm) and P-type (100) Si wafers. Before deposition, the substrates underwent a cleaning process in a sequence of acetone and ethanol, followed by drying with a dryer. The distance between the substrate and target was 10 cm. The chamber vacuum was exhausted to around 2.0×10^{-5} Torr, and then all substrates underwent etching and precleaning using an Ar$^+$ ion source for 40 minutes with a negative bias of 200 V. After the etching treatment, alternating deposition of Cr and GLC layers with Cr target and pure graphite target was used to produce the Cr/GLC multilayered coatings. The deposition procedures for the Cr and GLC layers were programmed for a single cycle, which was repeated eight times to achieve the Cr/GLC multilayered coating. The times for depositing the middle Cr, GLC, and top GLC layers were 4 minutes, 22 minutes, and 50 minutes, respectively. The detailed fabrication process of the Cr/GLC multilayered coating can be found in our previous studies [15,16].

2.2. Field exposure experiments

To ensure that only the surface featuring the deposited coating was exposed to seawater during the immersion experiment, the edges of the GLC-coated surface were sealed with epoxy resin. Fig. 1(a-b) illustrates the physical representation and schematic diagram of the encapsulated coated sample. The fixing holes were used to secure the sample and the cable, preventing sample loss during prolonged immersion. The deep-sea hanging panel experiments were conducted in collaboration with the research activities of the Dongfanghong −3 research vessel. The total immersion duration for the samples placed at the test points was 342 days. The coating sample deployment location was in the northwestern Pacific Ocean (at latitude 32°30.1377' N and longitude 149°11.2854' E). The samples were suspended at different depths using cables, with immersion depths of 500 meters, 1500 m, and 5942 meters, where 5942 m represented the maximum sea depth at the sample deployment point. To prevent sample loss and other unforeseen circumstances, five coating samples were placed at each depth. The encapsulated samples were securely fastened to the cable at their respective depths using nylon ropes. The schematic illustration of the sample deployment and the location of the sample deployment site are depicted in Fig. 1c. Pictures of the sample deployment and recovery site can be found in Supplementary figure S1.

During the immersion process, the variation in seawater temperature
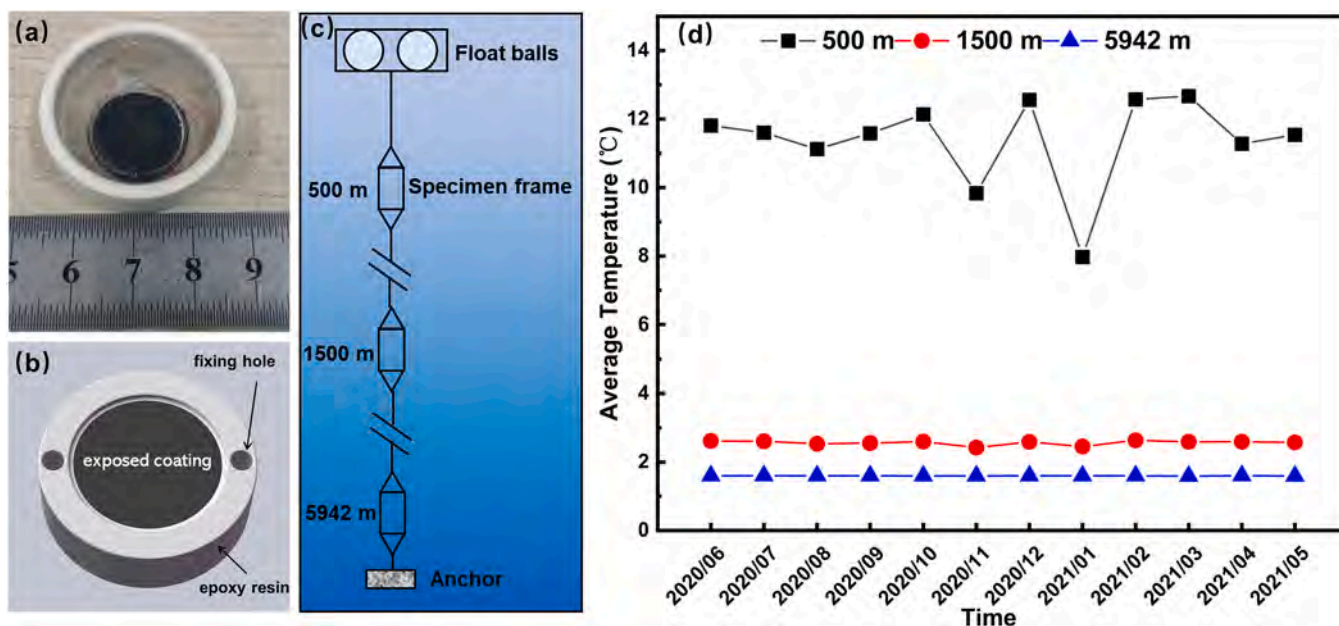

Fig. 1. (a) Physical and (b)schematic representation of encapsulated coating samples, (c) the sample delivery diagram , (d) Average seawater temperature monitoring values at different depths during the exposure.

is shown in Fig. 1(d). It is clear that the seawater temperature is highest at a depth of 500 m, with an average temperature of 11.39 ℃. The temperature dropped below 10 ℃ only in January 2021, which may have been ca used by ocean currents. At the depths of 1500 and 5942 m, there is relatively little variation in seawater temperature, with average values of 2.56 ℃ and 1.59 ℃, respectively. Temperature, as a crucial thermodynamic factor affecting electrochemical corrosion processes, may significantly impact coating performance due to these pronounced thermal contrasts. After concluding the deep-sea hanging panel experiments, the retrieved samples were dried and stored in a freezer at −80 ℃ to slow down their oxidation when exposed to air.

2.3. Sample characterization and testing analysis

Before conducting the characterization test, the epoxy resin was extracted from the samples, and any impurities adhering to the surface were removed by ultrasonic cleaning in alcohol and acetone. To determine the corrosion loss of the coating samples under the three immersion depths after the deep-sea hanging panel experiments, a weighing method was employed. Before encapsulation in epoxy resin, each sample was weighed three times using a high-precision electronic balance, and the average of these measurements was recorded as its pre-experiment weight. After completing the deep-sea hanging panel experiments, the samples, which underwent ultrasonic cleaning, were weighed three times, and the average was taken as their post-experiment weight. The difference between these two weights provided the corrosion loss result for each sample.

The surface corrosion morphology of the coatings was analyzed using optical microscopy and scanning electron microscopy (SEM), while the composition of the corrosion products was investigated using energy dispersive spectroscopy (EDS). The typical localized corrosion morphology and structural characteristics of the coatings were analyzed using focused ion beam (FIB) technology, in combination with EDS. The bonding states on the surface of the coating were characterized via Raman spectroscopy, and information on changes in sp^2 and sp^3 hybridized bonds was obtained by Gaussian fitting of the Raman spectra.

A corrosion-friction coupled experimental setup was utilized to test the coatings' frictional properties. The friction tests were performed with a 5 N load, 2 Hz frequency, 4 mm wear track length, and 1-hour friction time. After friction testing, the coating wear track cross-sections were measured with a profilometer. The wear rate for the coating samples at various immersion depths was then calculated using the wear rate formula provided below.

$$w = \frac{S \times l}{N \times L}$$

Where, S represents the wear track area (cm^2), l denotes the wear track length (cm), N stands for the applied load (N), and L represents the friction distance (m).

The electrochemical corrosion performance was tested with a Gamry electrochemical workstation. After the open-circuit potential had stabilized, electrochemical impedance spectroscopy (EIS) testing was carried out in a frequency range of 10^{-2} to 10^5 Hz with an AC perturbation potential of 10 mV. The results were analyzed by fitting with ZSimpWin software.
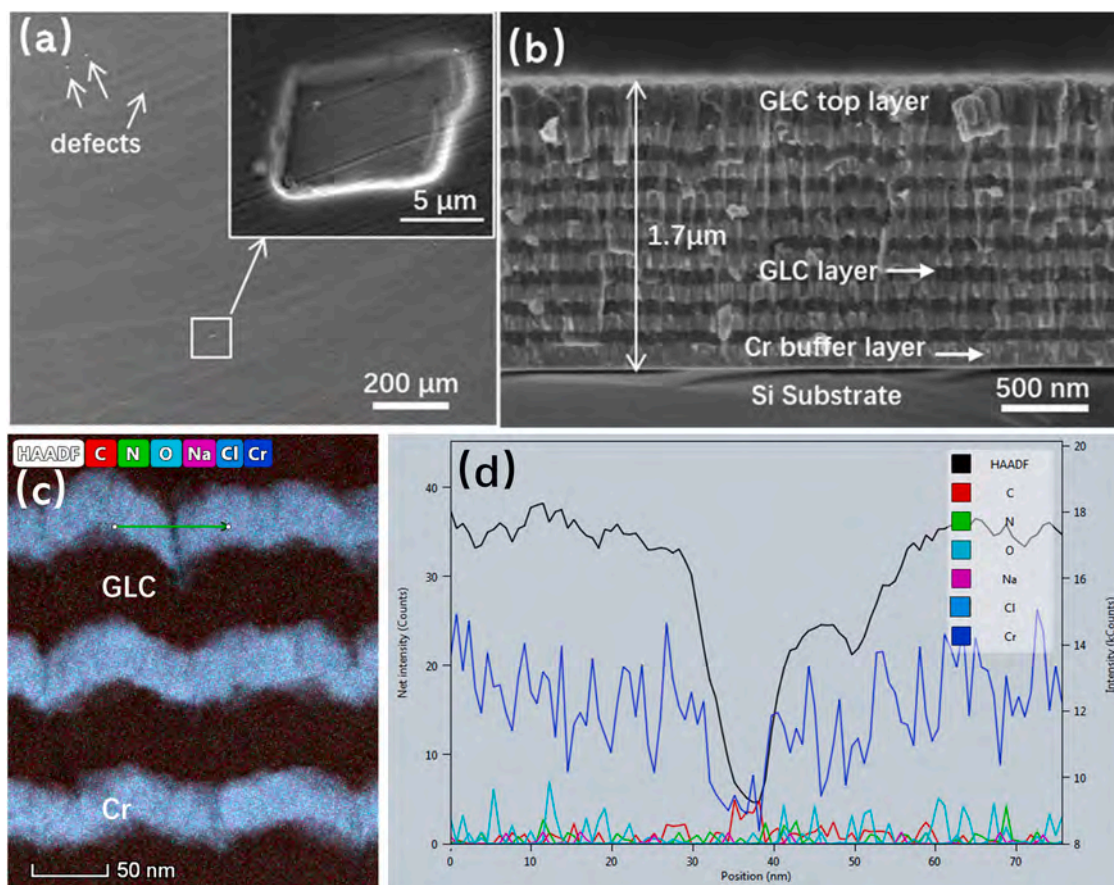

Fig. 2. The cross-sectional of the Cr/GLC multilayered coatings (a), the surface morphologies of the coatings and the defects (b) , the TEM-HAADF image of the multilayered coating after immersion at 5942 m (a) and (d) the line-EDS results obtained from (c) within the green lines.

3. Results

3.1. Cross-sectional and surface morphologies of the Cr/GLC multilayered coatings

Fig. 2 presents the surface and sectional structural images of the as-deposited Cr/GLC multilayered coating. The coating surface is largely uniform with localized micron-scale imperfections (indicated by white arrows) as shown in Fig. 2a. On enlarged inspection, these defects are mainly penetrating holes that exposed the substrate material. The cross-sectional view (Fig. 2b) demonstrates that the coating consists of alternating layers of Cr and GLC, with a total thickness of 1.7 μm. Small variations in the interlayer structure are presented due to the columnar growth of the underlying Cr transition layer. The structure of the immersed coating was analyzed additionally using the TEM-HADDF technique. The study revealed, (with particular emphasis on the columnar growth of the Cr layer indicated by the green line), significant undulations in the alternating structure of the coating. The line scan results provide clear evidence of localized Cr layer defects in this area. Further information on the interface structure and defect formation of the coating can be found in earlier research [15,16].

3.2. Components of the Cr/GLC multilayered coatings before and after exposure

Fig. 3 presents the Raman spectra of the as-deposited Cr/GLC coating samples and the exposed coatings at different depths, along with the corresponding fitting results. The Raman spectra analysis of the Cr/GLC coatings, after exposure at different depths, reveals the presence of two broadened peaks within the range of 900–1800 cm^{-1}. Through Gaussian fitting, it was discovered that all samples exhibited the characteristic of a strong D peak and a weak G peak, indicating the preserved structural features of typical graphitic coatings. From the fitting results, it is evident that the variation in the I_D/I_G ratio, representing the proportion of sp^2 and sp^3 hybridized states, exhibited only a minor increase, with values shifting from 3.55 to 3.63. Additionally, both the full width at half maximum (FWHM) of the G peak and the D peak didn't demonstrate discernible alterations. Previous research has indicated that amorphous carbon coatings may undergo corrosion reactions in corrosive environments with high chloride ion concentrations, leading to changes in their structural components [20]. However, the findings of this study suggest that in the deep-sea environment, amorphous carbon coatings did not undergo significant alterations in their structural components. Therefore, the protective performance of the coatings, in fact, primarily

originates from their excellent physical shielding effects.

3.3. The corrosion morphologies

3.3.1. Macroscopic morphology

The surface corrosion morphologies of the as-deposited coating and the Cr/GLC multilayered coatings after immersion at different depths were observed under low magnification and a wide field of view, with the results shown in Fig. 4. The results from Fig. 4a show that the surface of the as-deposited sample is smooth, flat, and without any visible defects like delamination or cracks. However, the surface of the coated sample exhibits varying degrees of coating delamination after immersion. At a depth of 500 m, several approximately circular corroded regions with scales of 100–200 μm became evident on the surface of the coating. This was accompanied by the onset of localized delamination, as indicated by the red arrows. After increasing the immersion depth to 1500 m, the corroded regions on the coating surface grew, leading to changes in their shape from nearly circular to irregular shapes that indicated the connected expansion of the corrosion areas. Upon further increasing the depth to 5942 m, localized corrosion and delamination
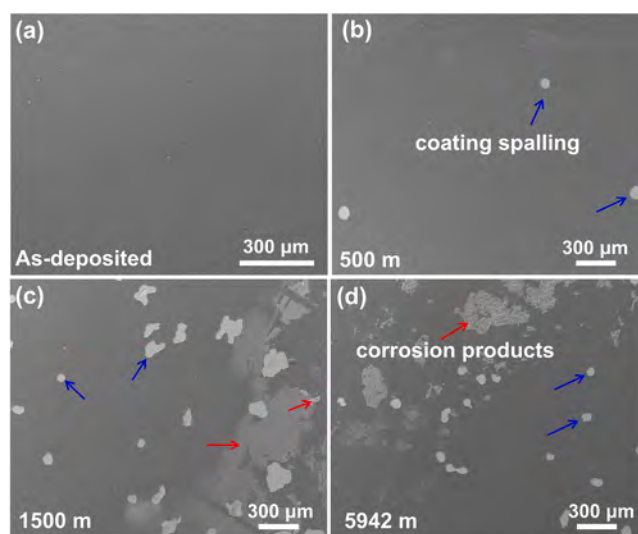

Fig. 4. Corrosion morphologies of Cr/GLC multilayered coating before and after exposure in different depths at Pacific Ocean.
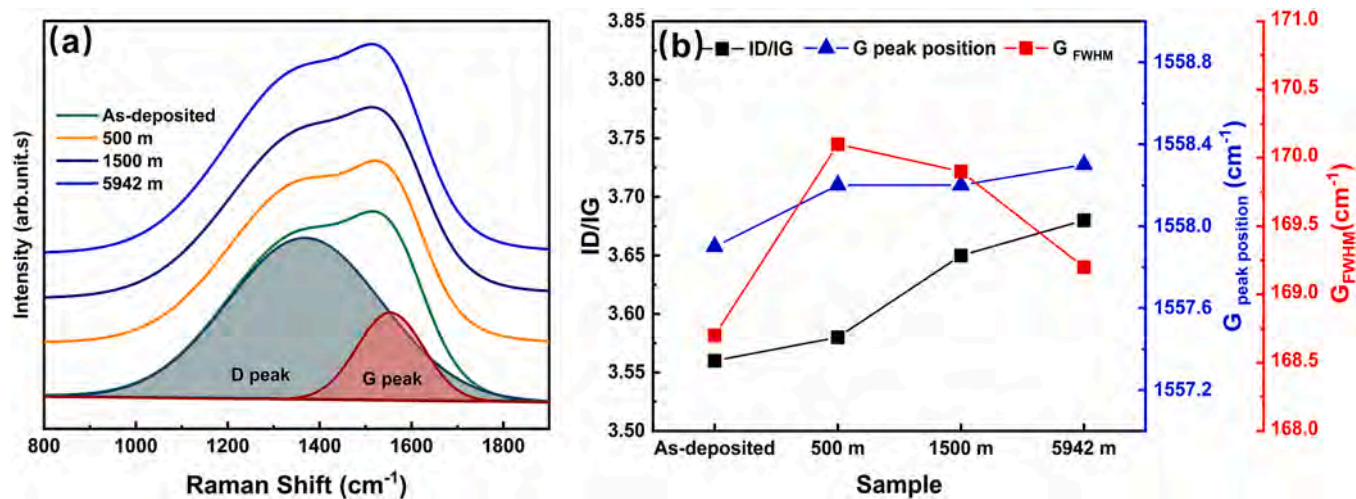

Fig. 3. (a) The Raman spectra for Cr/GLC multilayered coatings after exposure under different depth in Pacific Ocean, (b) the corresponding fitted result of I_D/I_G, $G_{position}$ and G_{FWHM}.

phenomena were similarly pronounced, and corrosion products began accumulating on the coating surface. Macroscopic surface corrosion morphologies indicated that coatings suffered significant corrosion at different immersion depths. In addition, as the depth of immersion increased, the occurrence of localized delamination and the outward diffusion of corrosion products on the surface of the coating became more pronounced.

The surface of the sample exposed to 5942 m shown in Fig. 4d presented various corrosion features such as localized corrosion at coating defects, coating delamination and substrate corrosion. Therefore, SEM and EDS were employed to further characterize and analyze the surface corrosion morphology and composition of the coatings. This approach aims to clarify the corrosion pathways and mechanisms of Cr/GLC multilayered coatings in deep sea environments.

3.3.2. Micromorphology analysis

A classification analysis was carried out based on the extent of surface corrosion in the coatings, including localized infiltration corrosion, corrosion-induced delamination of the coatings and corrosion of the substrate material.

Fig. 5 illustrates the typical localized spalling and several site of infiltration-corrosion morphology. Fig. 5b highlights the corrosion byproducts that are centered in the infiltrated area. Fig. 5c provides EDS mapping data derived from the region depicted in Fig. 5a. Due to the use of a backscattered electron-excited secondary electron mode, the morphology image presents both surface characteristics and information regarding elemental contrast. The dark areas in the morphology image do not display considerable structural alterations and are thus assumed to be the differences in elements. Furthermore, using an electron beam acceleration voltage of 20 kV, backscattered electrons can penetrate to the micron scale, suggesting that the contrast information could come from the interface at the base of the coating. Spectral analysis indicates significant enrichment of oxygen (O) and chromium (Cr) elements in both the central and peripheral regions of the dark area. Concurrently, the enrichment of Cl and Na elements is particularly noticeable at the center of the dark area. These characteristics indicate that, under the influence of hydrostatic pressure, seawater infiltrates the micro-defects in the coating, leading to corrosion at the interface between the coating and the substrate.

Fig. 6 illustrates a typical corrosion morphology that presents a localized spalling of the coating. The bottom of the spalled area is generally smooth, with a particular protrusion located at the center (highlighted by the white arrow). Two common penetrating defects are visible within the un-spalled section of the coating and on the left edge of the delamination. The edges of this area show noticeable indications of layered delamination, suggesting that corrosion is not restricted to the interface between the substrate and the Cr layer. Rather, it also transpires between the intermediate layers of Cr/GLC. The corrosion amongst the layers reduces the bonding strength and leads to the occurrence of the layered delamination phenomenon. This observation highlights that the process of penetration-corrosion may take place at the interface of the topmost Cr/GLC layers, as evidenced by the observed enrichment of oxygen (O) and chromium (Cr) elements. Fig. 6b showed a raised portion at the bottom of the penetrating defect, aligning with our prior research on defect formation. EDS mapping results (Fig. 6c) suggested that the defect fully exposed the substrate material, thereby allowing seawater to directly access the substrate through this pathway under hydrostatic pressure. Consequently, corrosion reactions would occur simultaneously within both the substrate material and the Cr layer. This feature of corrosion delamination indicates that the corrosion process initiates at the surface from localized penetrating defects, which then corrode preferentially at the interface in the substrate region. This progression ultimately leads to the gradual detachment of the coating around the penetrating defects. This explanation explains the nearly circular spalling morphology observed in the microscopy images shown in Fig. 4.

Severe localized corrosion on the coating surface, together with the corresponding EDS mapping results, is shown in Fig. 7. The corrosion morphology reveals pronounced corrosion beneath the delaminated coating. The EDS results indicate the diffusion and deposition of corrosion products, predominantly iron oxides, around the corroded pit. The magnified view depicted in Fig. 7b reveals significant substrate corrosion at the edge of the corroded pit, along with prominent coating cracking attributed to substrate/Cr interface corrosion. 17–4PH, being a precipitation-hardened martensitic stainless steel with numerous metallurgical carbide precipitates such as NbC and ε-Cu, is susceptible to notable localized corrosion due to the potential difference between these precipitates and the surrounding matrix[21]. Delamination results in the
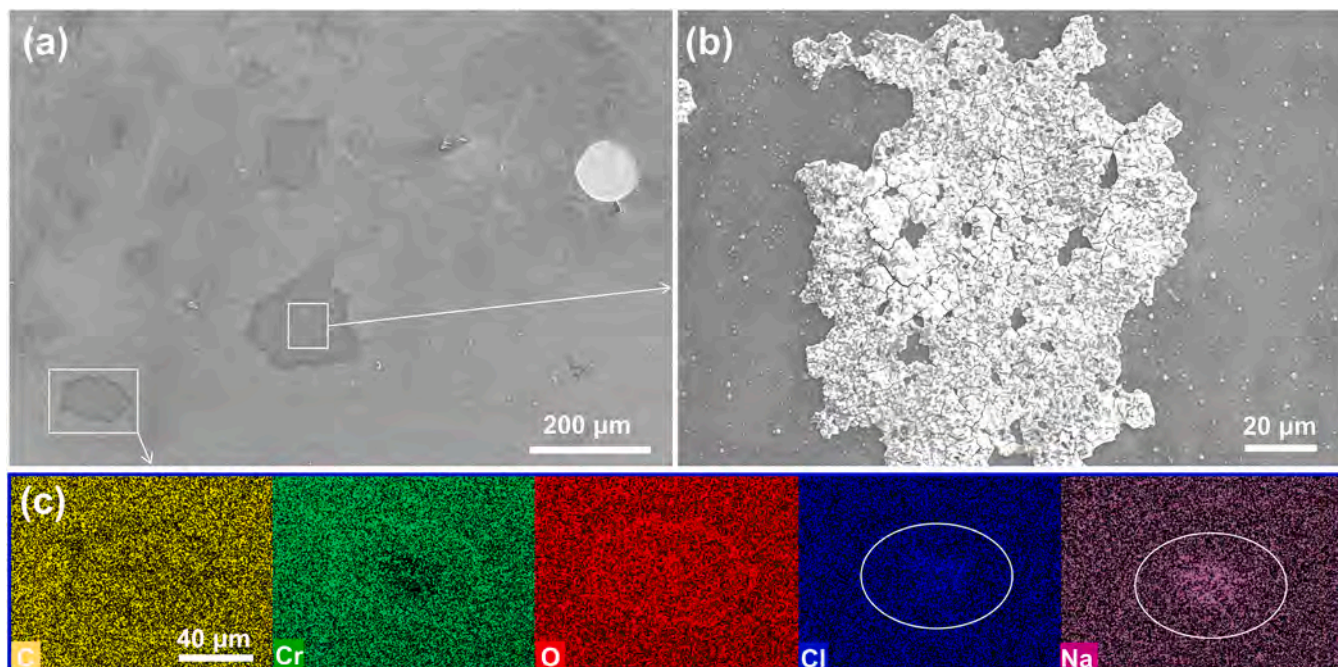

Fig. 5. The infiltration-corrosion morphology and EDS mapping results of Cr/GLC multilayered coating after immersion at 5942 m.
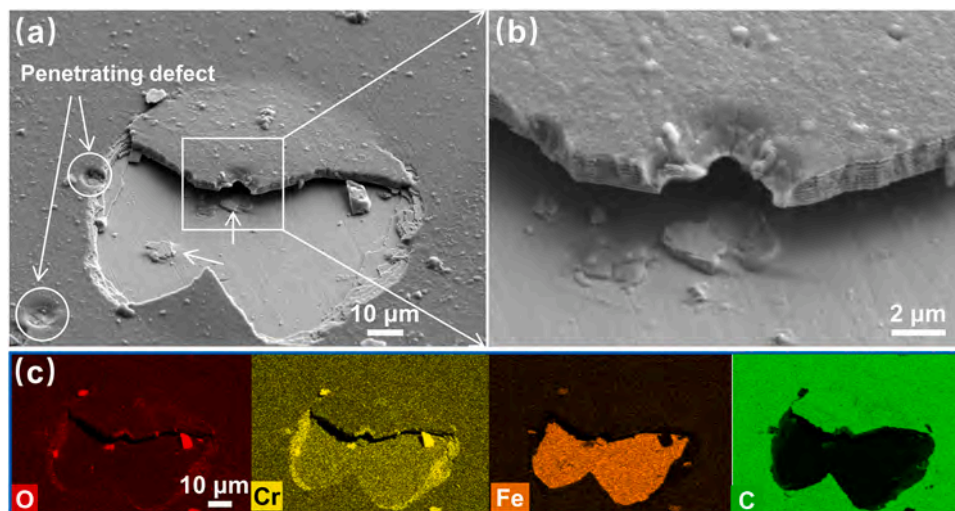
Fig. 6. (a-b) The local spalling of coating corrosion morphologies of Cr/GLC multilayered coating after immersion at 5942 m, (c) the corresponding EDS mapping results from (a).
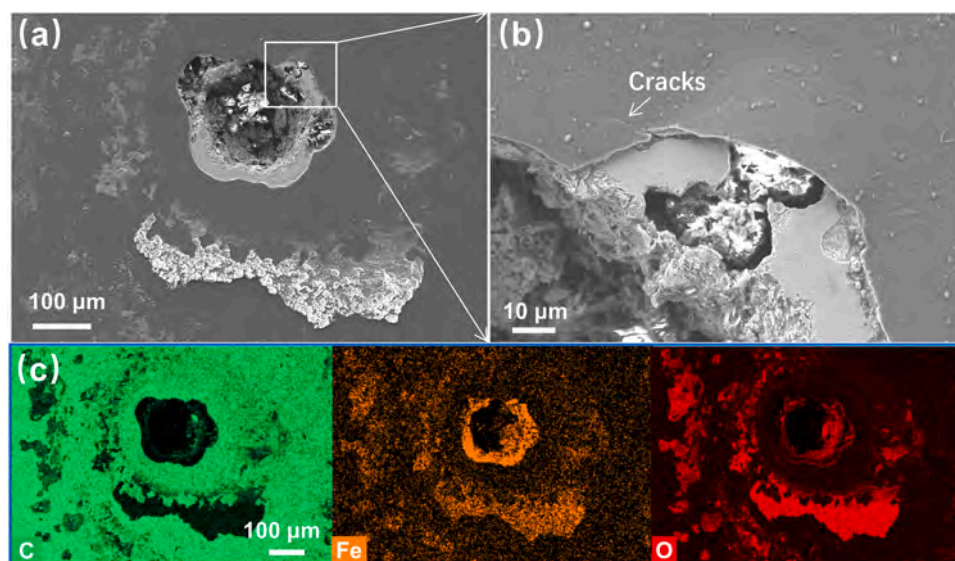

Fig. 7. (a-b) The severe localized corrosion morphologies of Cr/GLC multilayered coating after immersion at 5942 m, (c) the corresponding EDS mapping results from (a).

loss of the protective effect of the coating on the substrate and the resultant corrosion is primarily within the substrate. The products of localized substrate corrosion reactions cause pressure on the coating, causing it to crack and delaminate. Consequently, in the early stages of corrosion, interface corrosion dominates, leading to initial coating spalling and a significant increase in the exposed substrate area. After the distinctive organizational traits of the substrate, notable localized corrosion ensues. This event marks the commencement of coating delamination failure, with the accumulation and diffusion of substrate corrosion products serving as the main cause.

Considering the distinctive information from the previously mentioned corrosion morphologies, penetrating defects act as preferred locations for corrosion initiation within the coating. Corrosion reactions take place both at the base of these defects and at the interlayer interfaces. When the bonding strength between the substrate/Cr interface is reduced due to the accumulation of corrosion products, the considerable build-up of these products causes an upward protrusion of the entire coating, which ultimately leads to the cracking and delamination of the coating. Both the stainless steel substrate and the Cr transition

layer display excellent conductivity, and the inclination for galvanic corrosion between them is intensified under the hydrostatic conditions of the deep sea [22]. Thus, coating cracking and delamination due to corrosion product buildup at the interface are factual routes for coating failure. In addition, galvanic corrosion between the Cr interlayer and the adjacent GLC layer is induced by the large potential difference between Cr and GLC, resulting in weakened interlayer adhesion. Both coating spalling and interface corrosion have a significant impact on the corrosion protection and tribological performance of the coating. Coating spalling reduces its corrosion protection efficiency, while interface corrosion weakens the interfacial bonding performance of the coating, subsequently affecting its tribological properties.

3.4. Electrochemical corrosion behavior

Corrosion behavior of varying degrees was observed on the coating surfaces under different sea depth conditions, and this will have a significant impact on the corrosion resistance of the coatings. The results of electrochemical corrosion performance tests conducted on the Cr/GLC

multilayered coatings after exposure at different sea depths, are presented in Fig. 8. From the changes of the OCP, the initial unexposed samples present OCP of −0.04 $V_{Ag/AgCl}$, while after immersion, the OCP values of the three sample types declined significantly to around −0.11 $V_{Ag/AgCl}$ to −0.145 $V_{Ag/AgCl}$. As coating corrosion damage induced by deep-sea immersion is irreparable, OCP can be used as an indicator of the level of damage caused by coating corrosion[23]. Lower OCP values demonstrate that the structure of the coating has been impacted, resulting in a reduction in its effectiveness to protect against corrosion on the substrate. From both the Nyquist plot and Bode impedance magnitude plot, the capacitive arc radius and the impedance magnitude at low frequency $|Z|_{0.01}$ Hz of the samples have decreased
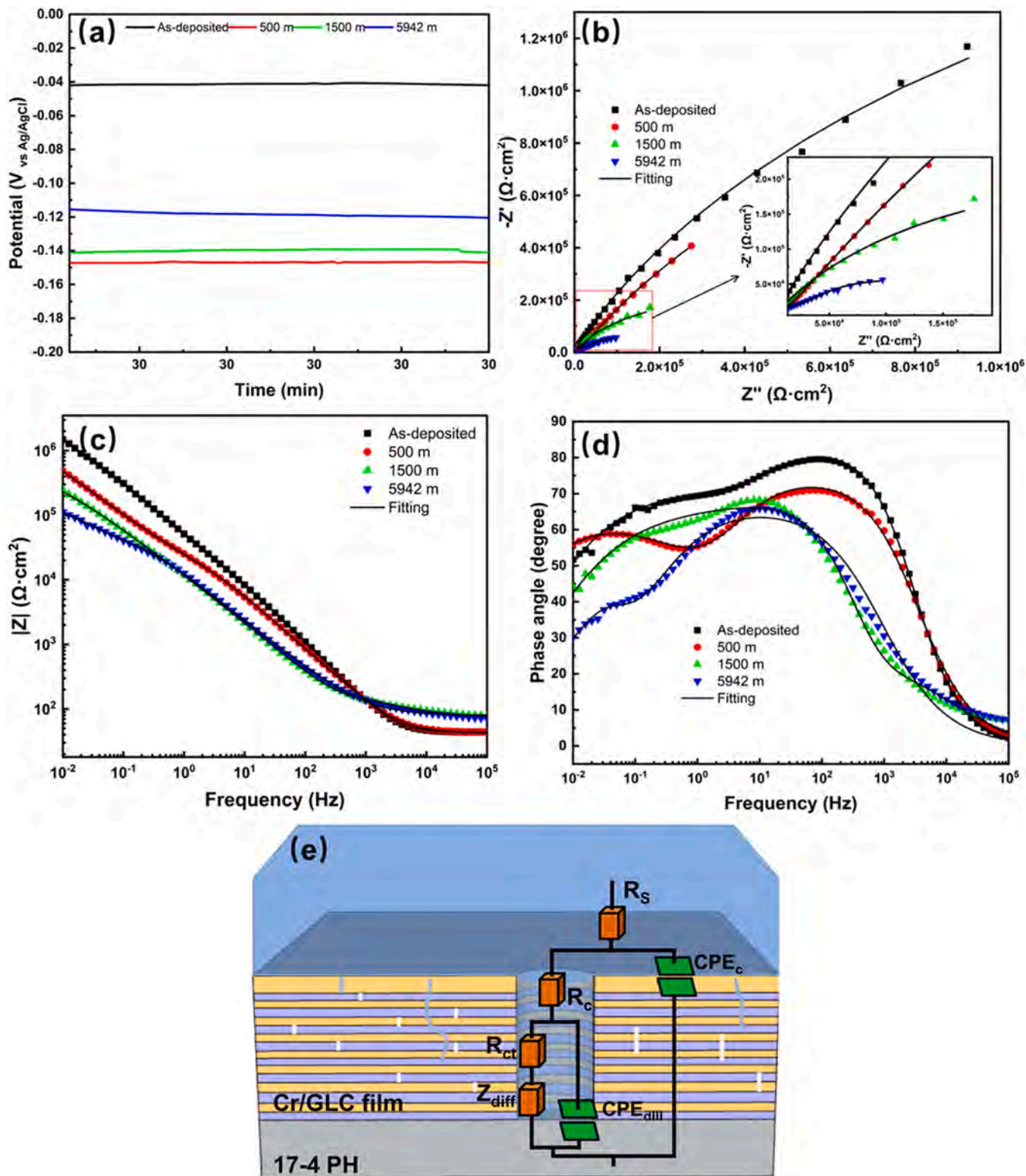

Fig. 8. The OCP values (a) and EIS results of Cr/GLC multilayered coating before and after an exposure in different depth at Pacific Ocean(b-d), the equivalent circuit used for fitting the EIS results (e).

substantially as compared to the as-deposited coating samples. The decrease is greater than one order of magnitude. This decline suggests that the coating's corrosion resistance has weakened significantly. The Bode phase angle graph indicates *a* gradual shift of the first phase peak towards lower frequencies accompanied by *a* decrease in peak value from roughly 80° to around 63° as immersion depth increases. Additionally, the phase angle drops to 30° in the most significant low-frequency range (<10 Hz). The low-frequency phase angle variability, which represents local corrosion resistance, demonstrates a considerable deficiency in coating protection, in accordance with the observed corrosion morphology, which is attributed to localized coating delamination. The Bode plot characteristics reveal two distinguishable time constant features of the substrate/coating system. Incorporating processes such as interfacial corrosion product diffusion, the fitting was carried out utilizing the equivalent circuit depicted in Fig. 8e. Within this circuit, R_s represents solution resistance, R_{po} represents pore resistance, R_{ct} denotes charge transfer resistance, and Z_{diff} characterizes the diffusion behavior of a semi-infinite plane. A Constant Phase Element (CPE) was implemented as a substitute for the ideal capacitor component. The solid black line indicate that the fitting results match well to the measured results over most frequency ranges, with chi-square values (χ^2) within the order of 10^{-4}, presenting a strong agreement between the chosen equivalent circuit and the actual EIS outcomes. Table 1 provides a summary of the fitting results.

Comparing the state after immersion to the as-deposited coating, it is apparent that both the pore resistance (R_{po}) and charge transfer resistance of the coated samples have significantly reduced following immersion. This indicates a gradual decrease in the corrosion protection capability of the coating. These results highlight that corrosion induced by immersion in real sea conditions causes permanent harm to the coating. During the immersion period, corrosion occurs, and it causes localized delamination of the coating, resulting in a compromised protective capability. Therefore, there is a considerable decrease in the ability of the corrosion resistance of the coatings.

3.5. Tribocorrosion preperformance

The coating samples showed extensive interfacial corrosion after immersion at various sea depths. This corrosion negatively affected the adhesion of the coating interface, and ultimately led to a reduced tribological performance (friction and wear) of the coating. To evaluate this effect, friction experiments were conducted under simulated seawater lubrication conditions. The results of the friction coefficient and wear rate are depicted in Fig. 9. Analysis of the monitoring data for Open Circuit Potential (OCP) revealed that the OCP immediately decreased upon sliding. OCP can reflect the ratio of the worn area to the intact area within the coating in the abrasion process [24]. The instantaneous decrease in OCP suggests that sliding process exposed more metal areas within the coating to the solution. In contrast, the samples deposited with original state showed only a minimal reduction of 0.05 V in OCP after sliding initiation, remaining stable until the end of the sliding test, when it returned to its initial level. This observation suggests that only minor damage was found in the as deposited coating during sliding. Additionally, the subsequent OCP recovery shows that exposed metal areas were able to repassivate swiftly.

The OCP of the exposed coating samples during the sliding tests showed a distinctive pattern. After the start of the sliding, the OCP first

dropped and then rose briefly before falling rapidly to its lowest point (from −0.42 V to −0.3 V) approximately 25 minutes into the test. This value approached the intrinsic value of the 17–4PH substrate, indicating total failure and delamination of the coating. The initial increase in OCP during the early stages of sliding was anomalous. This indicates the process by which the Cr/GLC multilayer coating filled the frictional interface due to delamination and abrasion, leaving the frictional interface relatively intact. In simple terms, the coating film was gradually ground into the friction interface by friction. This resulted in an increase in the OCP of the coating. Subsequently, as wear continued, the contact surface gradually exposed the substrate material. Following the frictional slip, all the coating samples exhibited a significant passivation phenomenon after immersion, with the OCP gradually recovering and even exceeding the initial value. This passivation phenomenon provides direct evidence of the exposure of the stainless steel substrate and the structural changes in the wear debris resulting from the friction process [25]. Correspondingly, the friction coefficients showed a comparable variation pattern. As shown in Fig. 9b, the friction coefficient curve for the as-deposited samples remained smooth and stable (~0.09), whereas the post-immersion samples experienced substantial fluctuations and increases. After roughly 10 minutes of sliding, all post-immersion samples gradually increased in the coefficient of friction (COF), surpassing the values seen for the as-deposited coating samples. Amongst them, the coating sample immersion in 1500 m achieved a COF value of up to 0.41, signifying the full detachment of the previously transparent surface coating. From the wear profiles shown in Fig. 9c, it is evident that the coatings immersed at different depths exhibit wear depths equal to or exceeding the coating thickness. In particular, the sample immersed at a depth of 1500 m shows a maximum wear depth of approximately 5 μm, indicating complete delamination of the coating. Calculation of the wear rate shows that the coated samples exhibit wear rates after immersion that exceed those of the as-deposited coatings by two orders of magnitude, reaching a maximum value of 2.76×10^{-7} mm^3/Nm (as shown in Fig. 9d). The significant deterioration in the mentioned tribological performance metrics clearly indicates a significant degradation in the wear resistance of the coatings induced by immersion at different sea depths.

3.6. Tribocorrosion morphology analysis

A detailed analysis of the wear morphology and composition of Cr/GLC multilayered coatings subjected to immersion at different depths was carried out to elucidate the mechanism responsible for the deterioration in coating performance after immersion. Fig. 10 shows the wear track morphologies of the as-deposited coating, revealing inconspicuous wear boundaries with a width of approximately 268 μm. Profilometry measurements indicate a wear depth of approximately 200 nm (Fig. 9c), suggesting that the coating remained intact without penetration. The microscopic areas of the wear tracks show significant grooving along the sliding direction, but no cracking or peeling of the coating. The EDS mapping results at the bottom of the wear track (Fig. 10c) show only C element enrichment in the sliding direction, while elements of the substrate material (e.g. Fe elements) are not enriched , indicating that the coating has not worn away.

However, the situation is quite different when the Cr/GLC multilayered coating samples were exposed to deep sea. As shown in Fig. 11, after immersion at a depth of 500 m, the coating exhibits a widened

Table 1
The fitting results of EIS for the coating after immersion test under various depth.

Time h	R_s Ω·cm^2	CPE_c μF·cm^{-2}	n_c	R_p kΩ·cm^2	CPE_{dll} μF·cm^{-2}	$n_{(c+o)}$	R_{ct} MΩ·cm^2	$W \times 10^{-7}$ Ω·s$^{0.5}$· cm^2	$\Sigma\chi^2 \times 10^{-4}$
As-deposited	42.35	2.13	0.94	23.2	2.74	0.66	5.07	21.5	1.62
500 m	42.2	5.19	0.84	30.9	98.4	0.67	3.57	15.1	3.48
1500 m	73.9	19.4	0.74	1.2	38.3	0.92	0.54	0.11	1.55
5942 m	76.9	19.3	0.74	6.7	86.6	0.89	0.07	0.02	4.86

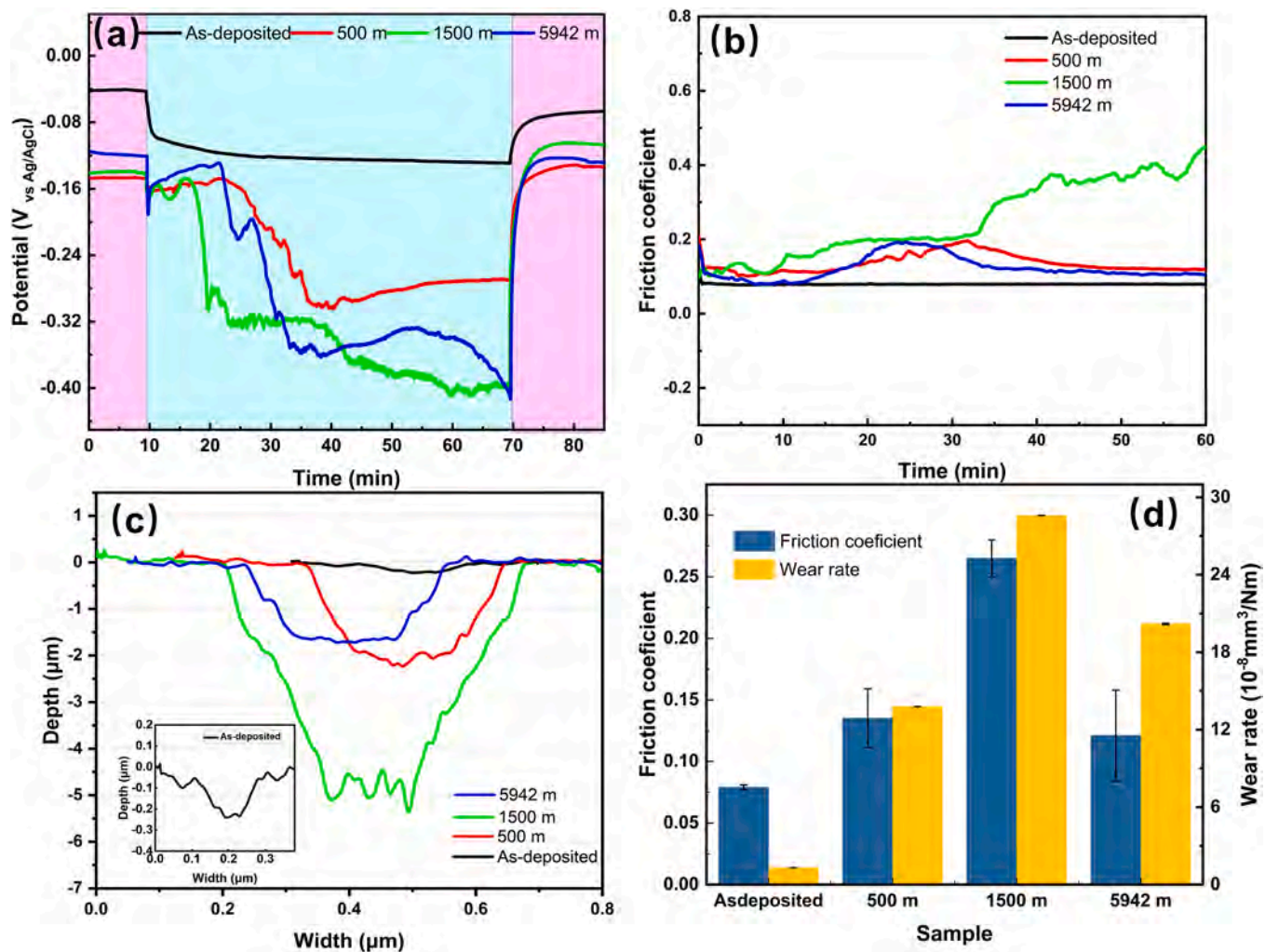**Fig. 9.** The monitored OCP value (a) and (b)friction curves during the sliding process of Cr/GLC multilayered coating during the sliding process, (c) the wear profiles of the coatings after the friction test and (d) the average friction coefficient and calculated wear rate.
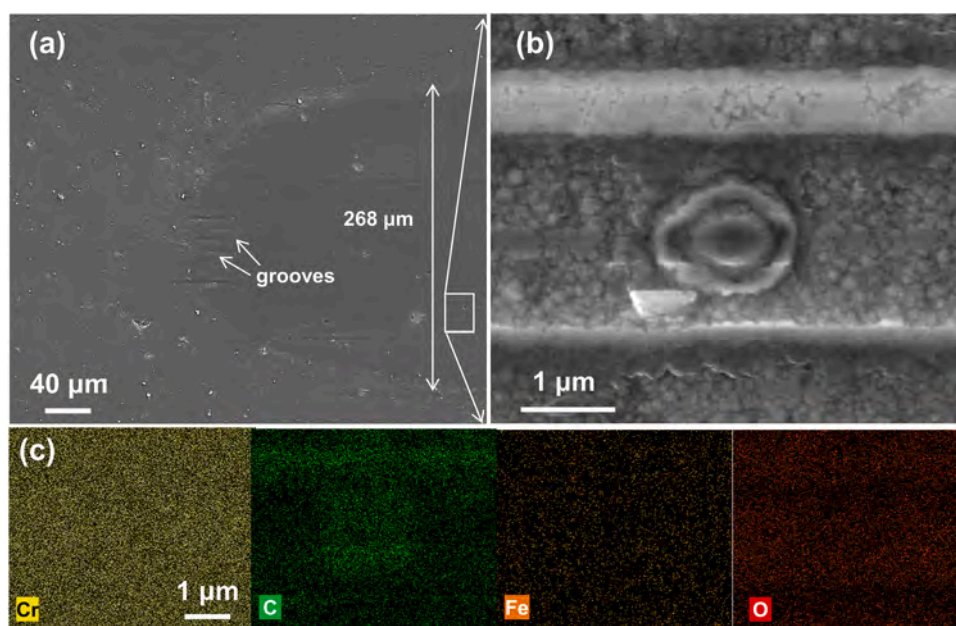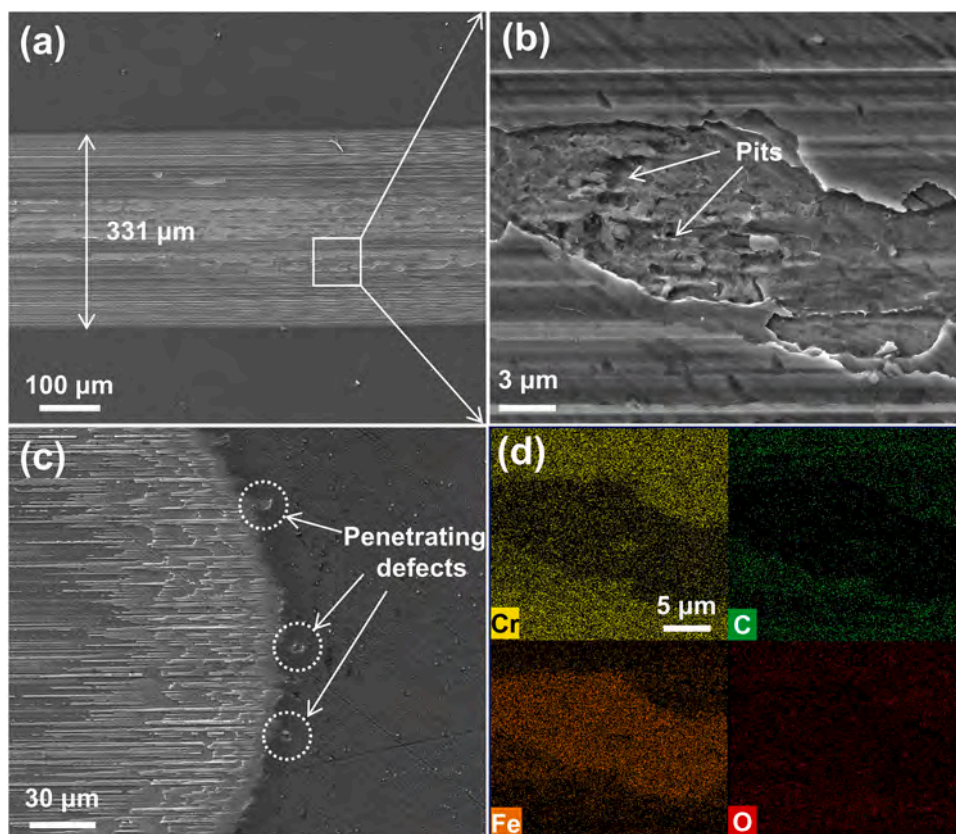

Fig. 10. The wear track morphologies (a-b) and (c) EDS mapping results of the as-deposited Cr/GLC multilayered coating after sliding test.

Fig. 11. The wear track morphologies of the Cr/GLC multilayered coating immersed at 500 m depth (a-c), the corresponding EDS mapping results from wear track (d).

wear track of 331 μm in width, with prominent wear features oriented parallel to the sliding direction. Detailed examination of the base of the wear track (Fig. 11b) and EDS analysis reveals central delamination within the base region of the coating, leaving remnants of the Cr layer at the margin. Close inspection of the delaminated region reveals that the exposed stainless-steel substrate is no longer smooth but riddled with numerous pits. Obviously, these localized pits are not the result of friction and must be attributed to severe interfacial corrosion that has occurred at this specific location within the coating. During immersion, seawater infiltrates the substrate-coating interface through defects, initiating interfacial corrosion and consequently compromising the adhesion of the coating. This in turn makes the coating highly susceptible to delamination at the interfacial corrosion site during frictional sliding, as proved by the pronounced delamination features at the bottom of the wear profile. In addition, at the edges of the wear track (as shown in Fig. 11c), the coating exhibits noticeable delamination during the frictional delamination process, accompanied by obvious through-thickness defects, indicating that these defect locations are areas of weakened coating adhesion. The frictional process rapidly leads to failure of the coating delamination at these locations, resulting in an increase in the coefficient of friction and the rate of wear. This friction morphology also illustrates that the short-term increase in OCP during the early stages of sliding is due to the filling effect resulting from coating delamination [26,27].

Fig. 12 displays the wear profile and elemental distribution of the coating sample following immersion at a depth of 1500 m. As shown in Fig. 12a, the wear width measures 503 μm, while the wear depth is 5 μm. Compared to earlier cases, the bottom of the wear track shows numerous grooves oriented parallel to the sliding direction, and there are noticeable localized delamination phenomena at the edges of the wear track. A thorough inspection of the delamination occurring at the edges of the wear track reveals remarkable interfacial corrosion characteristics. The

accumulation of corrosion products at the interface impairs the adhesive strength of the coating, leading to gradual delamination during the friction process. It is worth mentioning that Fig. 12c illustrates a considerably extensive delamination region at the edges of the wear track. Analysis of the delamination region at the edges of the wear track (Fig. 12 d) indicates distinct layering delamination characteristics. In combination with the EDS results, a significant accumulation of corrosion products is observed at the stainless steel/Cr buffer layer interface. Despite not being part of the frictional contact area, the extensive delamination present in this region indicates severe multi-interface corrosion, which significantly compromises the adhesion of the coating. As this sample demonstrates the maximum wear depth, its wear rate also reaches its highest value.

Following immersion at a depth of 5942 m, the wear profile of the coating sample is shown in Fig. 13 with a measured width of 321 μm. Significant delamination in the bottom of the wear track is observed. Combined with the microscopic morphology and EDS mapping results (Fig. 13b-c), the bottom of the coating shows obvious corrosion product accumulation and cracking, indicating that corrosion has occurred at this location. And similar localized defective corrosion and spalling phenomena also existed at the end of the wear mark (Fig. 13d). Notably, these morphological features resemble those of coating samples subjected to immersion at other depths, displaying a similar delamination failure mode resulting from interfacial corrosion damage.

In conclusion, it is apparent that coating samples, which have been exposed to various deep-sea conditions, are subject to interfacial corrosion due to seawater penetration. This type of corrosion leads to coating delamination, mainly due to inadequate interfacial bonding. As a result, the corrosion resistance and tribological properties of the coatings are affected adversely, which is an irreversible damage after the immersion. From a tribological perspective, it is noted that there is no clear connection between frictional performance and immersion depth.
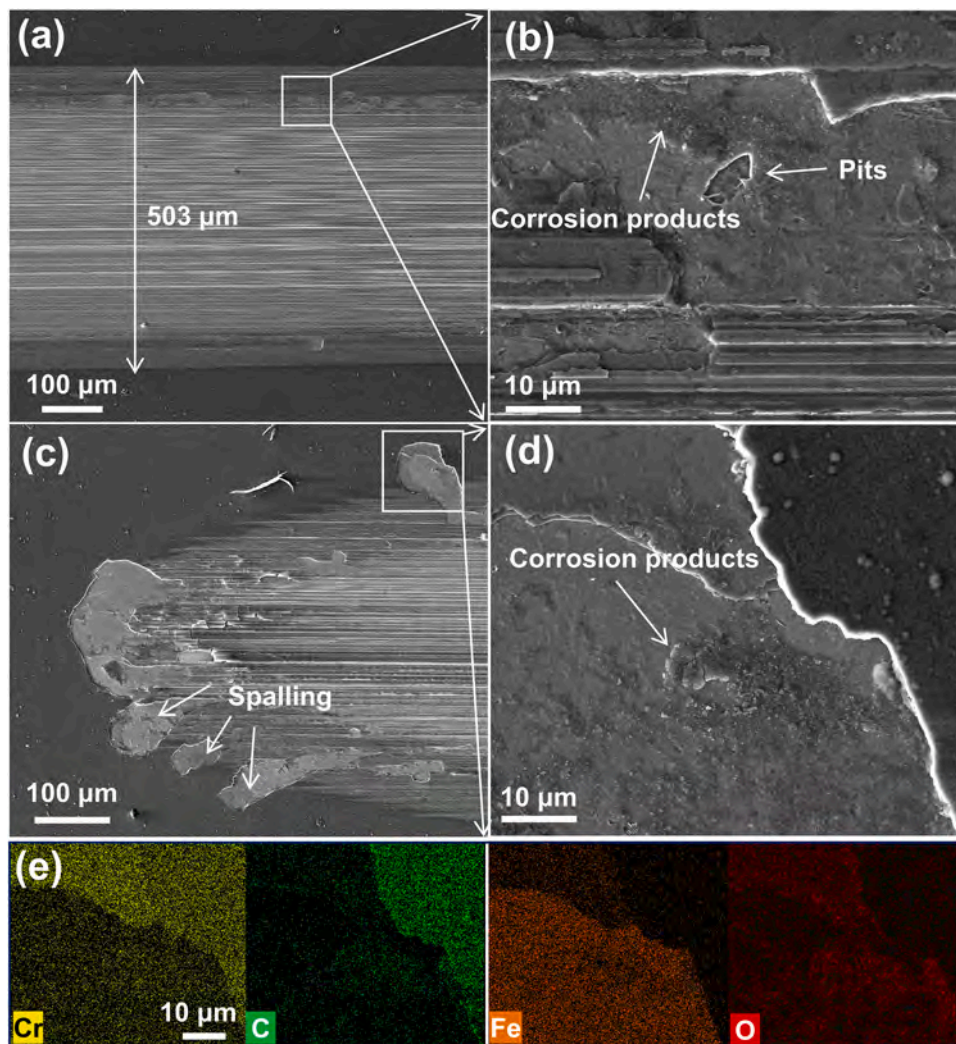
Fig. 12. The wear track morphologies of the Cr/GLC multilayered coating immersed at 1500 m depth (a-d), the corresponding EDS mapping results from wear track (e).

Although the wear rate reached its maximum value after immersion at 1500 m, all post-immersion samples exhibited a significant degradation in abrasion resistance. Moreover, the prevailing failure mechanism detected in these coatings can be ascribed to the same underlying issue: decreased adhesion caused by interfacial corrosion, resulting in premature delamination during the frictional process.

4. Discussions

This study investigated the degradation mechanisms of corrosion and tribocorrosion in Cr/GLC multilayered coatings after a 342-days of real ocean exposure at varying depths in the Western Pacific deep-sea environment. Although earlier studies have explored the impact of hydrostatic pressure on the corrosion behavior of multilayered GLC coatings under laboratory simulation conditions, the influence of hydrostatic pressure accelerated corrosion process on the tribocorrosion properties of the solid lubrication GLC coatings have not been explicitly addressed.

In this study, it was found that pristine components of the amorphous carbon coatings remain unchanged after deep sea immersion, but the corrosion resistance (impedance modulus) of the Cr/GLC multilayered coatings drop by two magnitudes order compared to the as-deposited coatings. More importantly, wear rate of all the immersion coatings is two magnitudes more than that of the coatings without immersion. These findings indicates that corrosion resistance of the Cr/GLC

multilayered coating is indeed deteriorated under deep sea hydrostatic pressure conditions, and these corrosion processes further make its wear resistance decreased as well. Although Guido's [20] found evidence of the amorphous carbon film may undergo corrosion reactions itself in corrosive environments with high chloride ion concentrations, our Raman spectroscopy results confirmed that the inert GLC coating does not dissolve at different depth deep sea exposure and its whole corrosion resistance still originated from its physical shielding effects. Hydrostatic pressure is the most significant factor affecting the corrosion behavior of materials in the deep sea environment, which not only affects the electrochemical reaction process, but also promotes the diffusion and transfer of corrosive media in the coating [17]. Therefore, the coating densification is the most critical factor to its protective performance in deep sea environment. GLC Coatings prepared by magnetron sputtering can contain defects of different scales, such as pinholes, nodules, pits or penetrating defects shown in Fig. 2. Although several studies have delved into the mechanisms behind defect formation in PVD coatings and how these defects affect coating performance, the majority of this research has been concentrated on hard coatings, such as TiAlN, TiAl-TaN, and VN [28–30]. Previously, we used the FIB-SEM technology investigated the microstructure of the different defect formed in the Cr/GLC multilayered coatings and confirmed that the penetrating defects having the most significant effect on the corrosion properties of the coating due to their large size [16]. Fig. 4–7 reveal the diverse corrosion
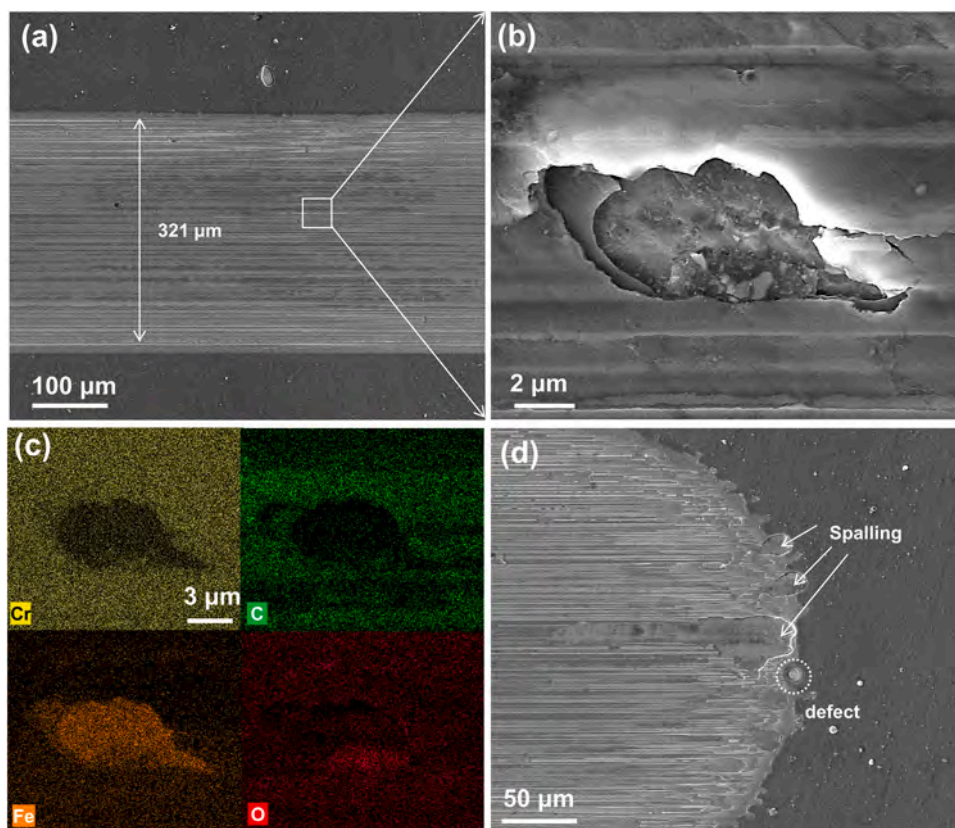
Fig. 13. The wear track morphologies of the Cr/GLC multilayered coating immersed at 5942 m depth (a-b), (c) the corresponding EDS mapping results from wear track (b), (d) the wear track morphologies at the end of the track.

morphologies observed in the coating after exposure to a depth of 5942 m. These images delineate the corrosion progression, which encompasses localized infiltration corrosion, the delamination of the coating layers, and the corrosion of the substrate material due to the intense hydrostatic pressure of the deep sea environment. Typically, such severe localized corrosion is only evident following anodic polarization tests, as documented in reference [20]. However, the coating samples in this study distinctly exhibit coating delamination due to localized corrosion through immersion experiments alone. This directly corroborates the corrosion mechanism involving hydrostatic pressure-accelerated local penetration. The ex-situ EIS results conducted on the Cr/GLC multilayered coatings after exposure at different sea depths indicate that the corrosion resistance reduced prominently, implying that corrosion damage sustained by the coating material during immersion is irreversible. These findings suggest that hydrostatic pressure is likely to further promote interfacial galvanic corrosion within multilayer coatings. Such corrosion-induced damage is likely to have a pronounced detrimental effect on their tribological performance.

Amorphous carbon coatings are recognized as efficient solid lubricants. The interlayer adhesion strength of the Cr/GLC multilayer coating is crucial for its wear resistance in deep-sea environments. The wear tracks observed on the GLC coatings following immersion at varying depths (illustrated in Figs. 11–13) suggest a dominant mechanism of coating delamination, which is closely associated with the galvanic coupling corrosion process at the interfaces, exacerbated by hydrostatic pressure. GLC coatings are extremely chemically inert and do not undergo corrosive chemical reactions in seawater environments and its corrosion potential is usually close to 0 V [31]. Higher sp^2 carbon content in GLC gives it good electrical conductivity. In this study, when Cr and GLC layers are alternately deposited to form a multilayered structured coating, the GLC layer serves as the cathode due to its corrosion potential as well as good conductivity, while the metallic Cr layer or the

exposed substrate material serves as the anode. Therefore, a galvanic couple is formed between the GLC-Cr layer or the GLC-substrate in the multilayered Cr/GLC coatings. It has been confirmed that deep-sea hydrostatic pressure has a significant effect on the corrosion of the galvanic. Ma's research found that, with the increase of hydrostatic pressure, the corrosion current of the anode Al in the Al/Fe galvanic couple pairs increased significantly, and the hydrostatic pressure can accelerate the corrosion process of the anode in the galvanic couple pairs [32]. Hu's results also confirm that the hydrostatic pressure can promote the corrosion process of the anode material in the galvanic coupling pairs [33]. Our recent research further confirmed that hydrostatic pressure promotes Cl- adsorption on the coating surface, which together promotes dissolution of the metal-transition Cr layer and the metal substrate [17]. Therefore, in the Cr/GLC multilayered coatings, the GLC layer is protected as the cathode while the metallic Cr layer or the exposed substrate material acts as the anode and undergoes continuous corrosion. According to the localized corrosion process, the interface galvanic corrosion failure mechanism of Cr/GLC coating under hydrostatic pressure condition is shown in Fig. 14. The possible reactions that may take place at the Cr layer and GLC are as follows:

$$Cr - 3e^- \rightarrow Cr^{3+} \tag{1}$$

$$2Cr + 3H_2O - 6e^- \rightarrow Cr_2O_3 + 6H^+ \tag{2}$$

$$2Cr^{3+} + 6H_2O \rightarrow 2Cr(OH)_3 + 6H^+ \tag{3}$$

$$H^+ + e^- \rightarrow H \tag{4}$$

Because the GLC-Cr galvanic coupling corrosion occurs at the coating defect location, the anodic process on the GLC layer and the cathodic process on the metal layer are negligible, namely only the cathodic reaction occurring on the GLC, while only the anodic reaction occurs on
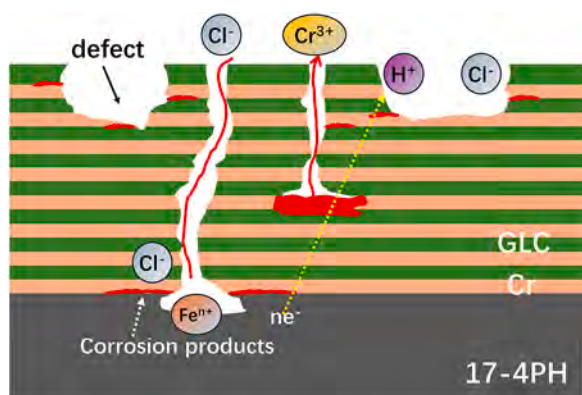
Fig. 14. The failure mechanism of Cr/GLC coating under hydrostatic pressure condition.

the Cr layer or the metal substrate. Assuming that S_{GLC} and S_{Cr} are the areas of GLC and Cr, respectively. In the seawater environment, its corrosion potentials satisfy $E_{GLC}>E_{Cr}$. When the two are coupled and galvanic coupling corrosion occurs, the new corrosion potential is Emix, and at this point satisfies $E_{GLC}>E_{mix}>E_{Cr}$. The GLC undergoes a cathodic reaction to produce a cathodic current, I_{GLC}, while the Cr undergoes an anodic reaction to produce anodic current I_{Cr}, then the galvanic current Ig can be expressed as [34,35]:

$$I_g = S_{GLC} \bullet I_{GLC} = S_{Cr} \bullet I_{Cr} \tag{5}$$

$$I_g = S_{GLC} \bullet \exp\left(\frac{E_{mix} - E_{GLC}}{\beta_{a,GLC}}\right) = S_{Cr} \bullet \exp\left(-\frac{E_{mix} - E_{Cr}}{\beta_{c,Cr}}\right) \tag{6}$$

where $\beta_{c,GLC}$ and $\beta_{a,Cr}$ are the cathodic Tafer slope for GLC and the anodic Tafer slope for Cr, respectively. As can be seen from Eqs. (5–6), the galvanic coupling current is closely related to the reaction area. In the coating defects occur in the location of the above galvanic corrosion reaction, due to the leakage of S_{Cr} area is very small, while the S_{GLC} area is relatively large. This structural feature will make the emergence of "big-cathode-small-anode" model, significantly increasing the anode Cr corrosion current I_{Cr}, which makes the Cr corrosion accelerated. Combined with the promoting effect of hydrostatic pressure on galvanic corrosion, for the exposed Cr/GLC multilayered coating samples, the hydrostatic pressure not only accelerated the seawater infiltration and diffusion process in the coating defects, but also produced a significant promotion of the corrosion process of the anode (Cr layer or substrate) in the galvanic coupling pairs formed by the GLC and the metal. The wear morphology of the coatings after wear and the characteristics of the coating delamination and spalling confirmed that the interfacial galvanic coupling corrosion commonly occurs in the samples after immersion. The friction experiments clearly confirmed that serious spalling failure occurred in all the coatings after immersion. The adhesion strength of GLC coatings significantly affects their tribological properties, and the occurrence of interfacial corrosion will seriously deteriorate the adhesion strength of the coatings when the corrosion at the defects evolves to the Cr-GLC interlayer interface or the substrate interface. Moreover, when the product accumulates to an adequate extent, the arising stress may lead to coating crack or even delamination. When external frictional shear forces are applied, the coating can easily peel away from the corroded location, as shown by the wear mark edge peeling feature in Fig. 12c.

It's important to note that there was no clear linear relationship between sea depth and the performance of the coating samples after immersion in deep sea at virous depths. This lack of linearity may be caused by the complex factors in the actual deep marine environment, such as hydrostatic pressure and temperature. Nevertheless, the overall trend indicates a significant decrease in the corrosion and tribological

performance of Cr/GLC multilayered coatings after immersion. It can therefore be concluded that the primary cause of the decline in tribological properties of the coatings is interfacial corrosion due to localized penetrating defects. Decreased adhesion strength due to interfacial galvanic coupling corrosion is unacceptable for solid lubricant coating materials of GLC coatings. Therefore, optimizing the deposition process to reduce the density of penetrating defects within the coating while increasing the sp^3 content in the amorphous carbon coating is a design guideline for the preparation of amorphous carbon coatings for deep sea applications.

5. Conclusions

This study compared the performance evolution and degradation mechanisms of Cr/GLC multilayered coatings over 342 days of real ocean exposure at three different depths in the Pacific Ocean. Mechanisms different from those observed in laboratory-simulated hydrostatic environments were revealed. Raman spectroscopy findings suggest that the pristine components structure of the amorphous carbon coating remains unchanged after seawater immersion. Nonetheless, a modification in the coating morphological structure of the coating is observed. Morphological analysis demonstrates that delamination layers occur in samples submerged at different depths, indicating corrosion at various interfaces within the substrate and the Cr transition layer. Furthermore, the immersion of coatings leads to a considerable reduction in the impedance modulus when local delamination occurs, dropping by two magnitudes compared to the as-deposited coatings. Corrosion across multiple interfaces worsens the interfacial adhesion strength. As a result, wear resistance is significantly reduced. The wear rate is two magnitudes more than that of the as-deposited coatings. Detailed analysis of the wear structures and EDS indicate that interfacial galvanic corrosion caused by localized penetrating defects within the coatings is responsible for the decline in the coatings' tribological performance. Therefore, it is essential to optimize the process with the aim of decreasing the density of penetrating defects. This is crucial in the design and manufacture of multilayered amorphous carbon coatings for deep-sea environments.

CRediT authorship contribution statement

Yingrui Liu: Writing – review & editing, Writing – original draft, Conceptualization. **Guanshui Ma:** Methodology, Investigation. **Xin Ma:** Resources, Methodology, Investigation. **Hao Li:** Methodology, Conceptualization. **Peng Guo:** Methodology. **Aiying Wang:** Writing – review & editing, Writing – original draft, Funding acquisition, Conceptualization. **Peiling Ke:** Writing – review & editing, Supervision, Investigation.

Declaration of Competing Interest

We confirm that the manuscript entitled "Corrosion and tribocorrosion performance degradation mechanism of multilayered graphite-like carbon (GLC) coatings under deep-sea immersion in the western Pacific" by Yingrui Liu, Guanshui Ma, Xin Ma, Hao Li , Peng Guo, Aiying Wang and Peiling Ke is an original work done by the authors. No conflict of interest exits in the submission of this manuscript, and the submission of the manuscript has been approved by all co-authors. This manuscript has not been published nor has it been submitted to any other journals or conference proceedings for consideration.

Data availability

No data was used for the research described in the article.

Appendix A. Supporting information

Supplementary data associated with this article can be found in the online version at doi:10.1016/j.corsci.2024.112418.

References

[1] S. Khamseh, E. Alibakhshi, B. Ramezanzadeh, M.G. Sari, A.K. Nezhad, Developing a graphite like carbon: niobium thin film on GTD-450 stainless steel substrate, Appl. Surf. Sci. 511 (2020), https://doi.org/10.1016/j.apsusc.2020.145613.

[2] X. Yin, J. Zhang, T. Luo, B. Cao, J. Xu, J. Chen, J. Luo, Tribochemical mechanism of superlubricity in graphene quantum dots modified DLC films under high contact pressure, Carbon 173 (2021) 329–338, https://doi.org/10.1016/j.carbon.2020.11.034.

[3] b Zechao Li a, Xiaoyan Guan b,c, Yongxin Wang b, J.L.b. *, Xiaoying Cheng a, Xia Lu b, Liping Wang b, Qunji Xue Comparative study on the load carrying capacities of DLC, GLC and CrN coatings under sliding-friction condition in different environments, (2018).10.1016/j.surfcoat.2017.04.065.

[4] M. Yan, X. Sui, X. Wang, S. Zhang, Y. Lu, J. Hao, W. Liu, Construction of a dense structure for GLC coatings by tailoring the nitrogen content to improve the aqueous-adaptability, Surf. Coat. Technol. 418 (2021), https://doi.org/10.1016/j.surfcoat.2021.127131.

[5] L. Li, P. Guo, L.-L. Liu, X. Li, P. Ke, A. Wang, Structural design of Cr/GLC films for high tribological performance in artificial seawater: Cr/GLC ratio and multilayer structure, J. Mater. Sci. Technol. 34 (2018) 1273–1280, https://doi.org/10.1016/j.jmst.2017.12.002.

[6] T. Duan, W. Peng, K. Ding, W. Guo, J. Hou, W. Cheng, S. Liu, L. Xu, Long-term field exposure corrosion behavior investigation of 316L stainless steel in the deep sea environment, Ocean Eng. 189 (2019) 106405, https://doi.org/10.1016/j.oceaneng.2019.106405.

[7] P. Traverso, E. Canepa, A review of studies on corrosion of metals and alloys in deep-sea environment, Ocean Eng. 87 (2014) 10–15, https://doi.org/10.1016/j.oceaneng.2014.05.003.

[8] S.H. Xing, Y. Li, J.A. Wharton, W.J. Fan, G.Y. Liu, F. Zhang, X.D. Zhao, Effect of dissolved oxygen and coupled resistance on the galvanic corrosion of Cr-Ni low-alloy steel/90-10 cupronickel under simulated deep sea condition, Mater. Corros. 68 (2017) 1123–1128, https://doi.org/10.1002/maco.201709473.

[9] H. Liu, J. Wang, P. Jiang, F. Yan, Hydrostatic pressure-dependent corrosion behaviour of polytetrafluoroethylene composites in the deep, Corros. Sci. 139 (2018) 289–300, https://doi.org/10.1016/j.corsci.2018.05.016.

[10] Y. Liu, J. Wang, L. Liu, Y. Li, F. Wang, Study of the failure mechanism of an epoxy coating system under high hydrostatic pressure, Corros. Sci. 74 (2013) 59–70, https://doi.org/10.1016/j.corsci.2013.04.012.

[11] W. Tian, L. Liu, F. Meng, Y. Liu, Y. Li, F. Wang, The failure behaviour of an epoxy glass flake coating/steel system under marine alternating hydrostatic pressure, Corros. Sci. 86 (2014) 81–92, https://doi.org/10.1016/j.corsci.2014.04.038.

[12] W. Tian, F. Meng, L. Liu, Y. Li, F. Wang, Lifetime prediction for organic coating under alternating hydrostatic pressure by artificial neural network, Sci. Rep. 7 (2017) 40827, https://doi.org/10.1038/srep40827.

[13] R. Liu, Y. Cui, B. Zhang, L. Liu, F. Wang, Unveiling the effect of hydrostatic pressure on the passive films of the deformed titanium alloy, Corros. Sci. 190 (2021), https://doi.org/10.1016/j.corsci.2021.109705.

[14] R. Liu, Y. Cui, L. Liu, F. Wang, Study on the mechanism of hydrostatic pressure promoting electrochemical corrosion of pure iron in 3.5% NaCl solution, Acta Mater. 203 (2021), https://doi.org/10.1016/j.actamat.2020.11.009.

[15] Y. Liu, H. Du, X. Zuo, P. Guo, L. Liu, K.-R. Lee, A. Wang, P. Ke, Cr/GLC multilayered coating in simulated deep-sea environment: corrosion behavior and growth defect evolution, Corros. Sci. 188 (2021), https://doi.org/10.1016/j.corsci.2021.109528.

[16] Y. Liu, S. Li, H. Li, G. Ma, L. Sun, P. Guo, P. Ke, K.-R. Lee, A. Wang, Controllable defect engineering to enhance the corrosion resistance of Cr/GLC multilayered coating for deep-sea applications, Corros. Sci. 199 (2022), https://doi.org/10.1016/j.corsci.2022.110175.

[17] H. Ma, R. Liu, Y. Cui, P. Ke, F. Wang, L. Liu, The effect law of different hydrostatic pressures on the failure of multilayer Cr/GLC coatings in 3.5 wt% NaCl solution, Corros. Sci. 217 (2023), https://doi.org/10.1016/j.corsci.2023.111120.

[18] K. Bobzin, N. Bagcivan, S. Theiß, R. Weiß, U. Depner, T. Troßmann, J. Ellermeier, M. Oechsner, Behavior of DLC coated low-alloy steel under tribological and corrosive load: effect of top layer and interlayer variation, Surf. Coat. Technol. 215 (2013) 110–118, https://doi.org/10.1016/j.surfcoat.2012.08.075.

[19] Z.X. Yang, B. Kan, J.X. Li, Y.J. Su, L.J. Qiao, Hydrostatic pressure effects on corrosion behavior of X70 pipeline steel in a simulated deep-sea environment, J. Electroanal. Chem. 822 (2018) 123–133, https://doi.org/10.1016/j.jelechem.2018.05.010.

[20] G. Reisel, G. Irmer, B. Wielage, A. Dorner-Reisel, Electrochemical corrosion behavior of carbon-based thin films in chloride ions containing electrolytes, Thin Solid Films 515 (2006) 1038–1042, https://doi.org/10.1016/j.tsf.2006.07.063.

[21] A. Barroux, N. Ducommun, E. Nivet, L. Laffont, C. Blanc, Pitting corrosion of 17-4PH stainless steel manufactured by laser beam melting, Corros. Sci. 169 (2020) 108594, https://doi.org/10.1016/j.corsci.2020.108594.

[22] S. Hu, L. Liu, Y. Cui, Y. Li, F. Wang, Influence of hydrostatic pressure on the corrosion behavior of 90/10 copper-nickel alloy tube under alternating dry and wet condition, Corros. Sci. 146 (2019) 202–212, https://doi.org/10.1016/j.corsci.2018.10.036.

[23] A.C. Vieira, L.A. Rocha, N. Papageorgiou, S. Mischler, Mechanical and electrochemical deterioration mechanisms in the tribocorrosion of Al alloys in NaCl and in NaNO3 solutions, Corros. Sci. 54 (2012) 26–35, https://doi.org/10.1016/j.corsci.2011.08.041.

[24] P. Henry, J. Takadoum, P. Berçot, Tribocorrosion of 316L stainless steel and TA6V4 alloy in H2SO4 media, Corros. Sci. 51 (2009) 1308–1314, https://doi.org/10.1016/j.corsci.2009.03.015.

[25] P. Ponthiaux, F. Wenger, D. Drees, J.P. Celis, Electrochemical techniques for studying tribocorrosion processes, Wear 256 (2004) 459–468, https://doi.org/10.1016/s0043-1648(03)00556-8.

[26] Y.P. Purandare, G.L. Robinson, A.P. Ehiasarian, P.E. Hovsepian, Investigation of High Power Impulse Magnetron Sputtering deposited nanoscale CrN/NbN multilayer coating for tribocorrosion resistance, Wear 452-453 (2020), https://doi.org/10.1016/j.wear.2020.203312.

[27] Y. Liu, S. Li, X. Zhou, P. Guo, R. Chen, J. Wei, A. Wang, P. Ke, Enhanced anti-tribocorrosion property of a-C film under high hydrostatic pressure by high power pulsed magnetron sputter (HiPIMS), J. Mater. Res. Technol. 28 (2024) 3052–3067, https://doi.org/10.1016/j.jmrt.2023.12.197.

[28] A. Drnovšek, P. Panjan, M. Panjan, M. Čekada, The influence of growth defects in sputter-deposited TiAlN hard coatings on their tribological behavior, Surf. Coat. Technol. 288 (2016) 171–178, https://doi.org/10.1016/j.surfcoat.2016.01.021.

[29] M. Fallqvist, M. Olsson, The influence of surface defects on the mechanical and tribological properties of VN-based arc-evaporated coatings, Wear 297 (2013) 1111–1119, https://doi.org/10.1016/j.wear.2012.11.012.

[30] M. Tkadletz, C. Mitterer, B. Sartory, I. Letofsky-Papst, C. Czettl, C. Michotte, The effect of droplets in arc evaporated TiAlTaN hard coatings on the wear behavior, Surf. Coat. Technol. 257 (2014) 95–101, https://doi.org/10.1016/j.surfcoat.2014.01.010.

[31] J. Wei, P. Guo, L. Liu, H. Li, H. Li, S. Wang, P. Ke, A. Wang, Tailored electrochemical behavior of ta-C film by glancing angle deposition, Appl. Surf. Sci. 516 (2020), https://doi.org/10.1016/j.apsusc.2020.146115.

[32] J. Qiu, A. Wu, Y. Li, Y. Xu, R. Scarlat, D.D. Macdonald, Galvanic corrosion of Type 316L stainless steel and Graphite in molten fluoride salt, Corros. Sci. 170 (2020), https://doi.org/10.1016/j.corsci.2020.108677.

[33] W.S. Tait, Chapter 5 - Electrochemical Corrosion Basics, in: M. Kutz (Ed.), Handbook of Environmental Degradation of Materials (Third Edition), William Andrew Publishing, 2018, pp. 97–115.

[34] R. Ma, Y. Shen, C. Wang, J. Dong, W. Ke, Effect of hydrostatic pressure on the thermodynamic and kinetic behavior of metal electrode reactions, Electrochim. Acta 424 (2022) 140617, https://doi.org/10.1016/j.electacta.2022.140617.

[35] S. Hu, R. Liu, L. Liu, Y. Cui, E.E. Oguzie, F. Wang, Effect of hydrostatic pressure on the galvanic corrosion of 90/10 Cu-Ni alloy coupled to Ti6Al4V alloy, Corros. Sci. 163 (2020), https://doi.org/10.1016/j.corsci.2019.108242.